Supporting Informations

Multiscale Engineering of Triple-Phase Catalytic Architecture: Integrating Atomic Fe-N_x Sites, Fe/Fe_3C Nanoclusters and $Ni(OH)_2$ Nanocrystals on S,N-Doped Carbon for Rechargeable Zn-Air Batteries

Tao Luo [a], Zhihao Yu [b], Jingyao Liang [a], Pengfei Wang [a], Zhouyang Long [a,*], Ping Zhu [a,*], Xinsheng Zhao [c,*], Sa Liu [a,*]

[a] *School of Chemistry and Materials Science, Jiangsu Key Laboratory of Green Synthetic Chemistry for Functional Materials, Jiangsu Normal University, Xuzhou 221116, China*

[b] *Cw Chu College, Jiangsu Normal University, Xuzhou 221116, China*

[c] *School of Physics and Electronic Engineering, Jiangsu Normal University, Xuzhou 221116, China*

---

[*] Corresponding author.
E-mail addresses: longzhouyangfat@163.com (Z. Long); zhuping@jsnu.edu.cn (P. Zhu); xinshengzhao@jsnu.edu.cn (X. Zhao); liusa@jsnu.edu.cn (S. Liu).

Experimental Section:

Materials

Iron(II) Acetate (>90.0%, Aladdin), Sodium citrate dehydrate (99.0%, Macklin), Thiourea and Urea (AR, Aladdin), 1,10-Phenanthroline monohydrate (≥99.0%), Nickel chloride hexahydrate (99.998%, Alfa Aesar), Sodium borohydride ($NaBH_4$, 99.5%, Sinopharm Chemical Reagent Co. Ltd.), Potassium hydroxide (KOH, AR, Sinopharm Chemical Reagent Co. Ltd.), Absolute ethanol (C_2H_5OH, 99.8%, Aladdin), acrylic acid (AA, ≥98%, Aladdin), N, N′-Methylenebisacrylamide (MBAA, ≥ 98%, Aladdin), potassium peroxodisulfate ($K_2S_2O_8$, AR, Aladdin), Sodium hydroxide (NaOH, AR, Sinopharm Chemical Reagent Co. Ltd.), were used as received without any further purification.

Materials characterization

Scanning electron microscopy (SEM) images were acquired on a HITACHI S-8010 electron microscope at an accelerating voltage of 15 kV. Transmission electron microscope (TEM) images with energy dispersive spectroscopy (EDS) were obtained with a JEM-2100F microscope at 120 kV acceleration voltage. Powder X-ray diffraction (XRD) measurements were conducted using a Bruker AXS D8 ADVANCE diffractometry with filtered Cu Kα radiation ($\lambda = 0.15406$ nm) between 10° and 80° at 40 kV and 40 mA. Raman spectra were measured by a LabRAM HR800 Laser Confocal Micro-Raman Spectroscopy using the laser-excitation wavelength of 532 nm. N_2 adsorption-desorption isotherms were tested at 77 K with a Quantachrome Autosorb IQ_2-VP instrument, and the samples were degassed at 100 °C for 12 h under vacuum before the measurements were taken. X-ray photoelectron spectroscopy (XPS) was performed on ESCALAB 250Xi (Thermo Fisher) with an Al

Kα (1486.6 eV) X-ray source. The element contents were determined by inductively coupled plasma optical emission spectroscopy (ICP-OES) on a SPECTRO GENESIS ICP spectrometer. ^{57}Fe Mössbauer spectrum was obtained with a 57Co:Rh source on a Topologic 500A spectrometer driving with a proportional counter at room temperature.

Electrochemical measurements

Electrochemical tests were carried out with a three-electrode system on the CHI 700E/660E electrochemical workstation (Chenhua, Shanghai). The catalyst ink was prepared by dispersing 5 mg of the resultant catalyst in a mixture solution of ethanol (0.6 mL) and Nafion (50 μL, 5 wt%, DuPont) under ultrasonication for about 1 h. All potentials were converted to the reversible hydrogen electrode (RHE) scale using the Nernst equation. The current densities for ORR and OER were calculated on the basis of glassy carbon disk area and carbon cloth area, respectively.

Oxygen reduction reaction (ORR) tests: A polished rotating ring-disk electrode (RRDE) of glassy carbon (GC) (4 mm in disk diameter, 5 mm in ring inner diameter and 7 mm in ring outer diameter, ALS Co., Ltd., Japan), Pt foil and Hg/HgO electrode (in 0.1 M KOH) acted as the working, the counter and the reference electrodes, separately. 10 μL of the catalyst ink was pipetted onto the pre-polished GC electrode to generate a catalyst loading of 612 μg cm^{-2} and was dried at room temperature. Prior to electrocatalytic measurements, the electrolyte solution was purged with N_2 or O_2 for at least 30 min. Before the formal measurements, all the working electrodes were firstly activated by accelerated cyclic voltammetry (CV) process between 0 and 1.2 V in N_2-saturated 0.1 M KOH electrolyte at a sweep rate of 100 mV s^{-1} until the curve stabilized. CV curves were performed in both N_2-saturated and O_2-saturated 0.1 M KOH at 50 mV s^{-1}. Thereafter, the ORR LSV curves were obtained at different rotation speeds (400, 625, 900, 1225 and 1600) and at a scan rate of 10 mV s^{-1} in O_2-saturated 0.1 M KOH electrolyte, and calibrated by the background current in N_2-saturated 0.1 M KOH electrolyte. Electrocatalytic stability was conducted by cycle voltammetry with the potential range of 0.6−1.0 V at a scan rate of 100 mV s^{-1} in 0.1 M O_2-saturated electrolyte. For comparison, the commercial Pt/C was also measured with Pt loading of 20 μg cm^{-2}.

The Koutecky-Levich (K-L) equation is widely applied to investigate the ORR kinetics, which can be described as follows

$$j^{-1} = j_k^{-1} + j_d^{-1} = j_k^{-1} + (B\omega^{1/2})^{-1} \tag{1}$$

$$B = 0.2nFC_0D_0^{2/3}v^{-1/6} \tag{2}$$

where j, j_k and j_d are the measured, kinetic and diffusion-limiting current densities (mA cm^{-2}), respectively; ω is the rotation rate of the electrode (rpm); and B is the Levich slope calculated from equation (2), n is the electron transfer number per O_2 molecule, F is the Faraday constant (96485 C mol^{-1}); A is the area of glassy carbon electrode (cm^{-2}); C_0 is the bulk concentration of O_2 (solubility) in 0.1 M KOH (1.2×10^{-3} mol L^{-1}); D_0 is the diffusion coefficient of O_2 in 0.1 M KOH (1.9×10^{-5} cm^2 s^{-1}); v is the kinetic viscosity of 0.1 M KOH (0.01 cm^2 s^{-1}). The constant 0.2 is adopted when the rotation speed is expressed in rpm.

To monitor the formation of peroxide during ORR, RRDE was performed in O_2-saturated 0.1 M KOH electrolyte. The disk electrode was scanned at a rate of 10 mV s^{-1}, while the Pt-ring potential was set at 1.2 V versus RHE constantly. The hydrogen peroxide yield (%H_2O_2) and electron transfer number (n) per O_2 molecule were calculated from the following equations, respectively:

$$\%H_2O_2 = (200i_r/N)/(i_d + i_r/N) \tag{3}$$

$$n = 4i_d/(i_d + i_r/N) \tag{4}$$

where i_d, i_r and N correspond respectively to the measured disk current, ring current and electrode collection efficiency of the Pt ring (0.424).

Oxygen evolution reaction (OER) tests: A graphite carbon plate and Hg/HgO electrode (in 1.0 M KOH) were employed as the counter and the reference electrodes, respectively. And the as-prepared catalysts modified carbon cloth (CC) with a window size of 1.0 cm × 1.0 cm was used as the working electrode with a loading of 0.8 mg cm^{-2}. The LSV curves of the catalysts were recorded from 1.1 to 1.8 V at a scan rate of 10 mV s^{-1} in O_2-saturated 1.0 M KOH electrolyte, which were manually corrected for solution resistance according to the equation: $E_{\mathrm{corrected}} = E_{\mathrm{measured}} - iR_s$, where i is the measured current, and R_s is compensated ohmic resistance of the electrolyte from the fittings of the electrochemical impedance spectrum (EIS). EIS tests were conducted with an AC voltage at 5 mV amplitude in a frequency range from 1×10^6 Hz to 1×10^{-2} Hz at 1.62 V. The double-layer capacitance (C_{dl}) is proportional to electrochemical surface area (ECSA), which is generally used to evaluate the effective ECSA. To estimate the C_{dl} of the catalyst, CV curves were measured in a non-Faradic region between 1.13 and 1.19 V *vs*. RHE at different scan rates (0.02, 0.04, 0.06, 0.08 and 0.10 V s^{-1}). Then, the plots of $(i_a - i_c)/2$ (where i_a and i_c denote the anodic and cathodic currents (mA) recorded at a potential of 1.16 V *vs*. RHE from CV curves) against different scan rates were obtained, and their linear slopes were regarded as the values of the C_{dl} (mF cm^{-2}).

The ECSA (cm^2) is calculated by the following equation [5]:

$$ECSA = C_{dl}/C_s \tag{5}$$

C_s denotes the specific capacitance of a flat, smooth surface of the electrode material, which is assumed to be 0.04 mF cm^{-2} based on previously reported electrocatalysts [S1, S2].

The long-term potential-time (E-t) test at 10 mA cm^{-2} was used to investigate the stability of catalysts for OER.

Assembly and performance test of Zn–air batteries: A homemade liquid ZAB was assembled by a polished zinc plate as the anode, a 1.0 cm^2 window area of carbon cloth (CC) attached with gas-diffusion layer (GDL) loaded with 2.0 mg catalyst as an air-cathode, and 6.0 M KOH containing 0.2 M zinc acetate as electrolyte. For comparison, the mixture of commercial Pt/C and RuO_2 (mass ratio of 1:1) was also as the cathode electrode catalyst with a same loading.

The quasi-solid-state ZAB was assembled with a sandwich structure: $Ni(OH)_2$/FeNC/SNC loading GDL as the cathode, Zn foil as the anode, and a gel of alkaline sodium polyacrylate (PANa) containing KOH/zinc acetate as the quasi-solid-state electrolyte. The gel electrolyte was prepared according to the following procedure. 7.2 mL AA was mixted with 15 mL deionized water, and then 4 g NaOH was added into the solution in ice-water bath and stirred vigorously. Subsequently, MBAA (10 mg) and $K_2S_2O_8$ (50 mg) were added into the cool solution in sequence. After degassed under static conditions, the solution was poured into a petri dish, and polymerized at 60 ^{o}C for ~45 min to obtain the PANa gel. Finally, the PANa was immersed into 6.0 M KOH containing 0.2 M zinc acetate for ~24 h to obatin the gel electrolyte.

With CHI 660E electrochemical workstation, the open circuit voltage curves were measured, and the polarization curves of charge and discharge were also performed by the LSV method at a scan rate of 1 mV s^{-1}. The charge−discharge cycling test was conducted on LAND battery testing station (Wuhan LAND Electronic Co. Land). The duration of each cycle was set to 30 min (15 min for discharging and 15 min for subsequent charging).

The zinc foil was weighed before testing the cross-current discharge curve and then weighed again after the test was completed to record the mass of zinc consumed during the reaction. The specific capacity C (mAh g^{-1}) of zinc−air batteries are calculated using the formulas shown below:

$$C = \frac{I \times t}{m_{Zn}} \tag{6}$$

where I is the applied current, t is the discharge time, m_{Zn} means the mass of consumed zinc.

Theoretical calculations

Density functional theory (DFT) calculations were performed using CP2K package version-2022.1 [1] with the Gaussian Plane Wave method in the QUICKSTEP module [2]. The PBE [3] exchange-correlation functional with Grimme-D3 [4-5] dispersion correction was employed. Double-zeta valence polarized sets and GTH [6-8] pseudopotentials were used. Plane wave and relative cut-offs were 400 and 55 Ry, respectively, with SCF convergence criteria set to 2.0 × 10^{-6} Ha. A 15 Å vacuum gap was used to avoid interactions between periodic images. Surface structures were optimized at the Γ point, with root mean square and maximum force convergence set to 3.0 × 10^{-4} and 4.5 × 10^{-4} Ha·Å^{-1}, respectively. Density of states were analyzed with

MULTIWFN [9-10].

Results

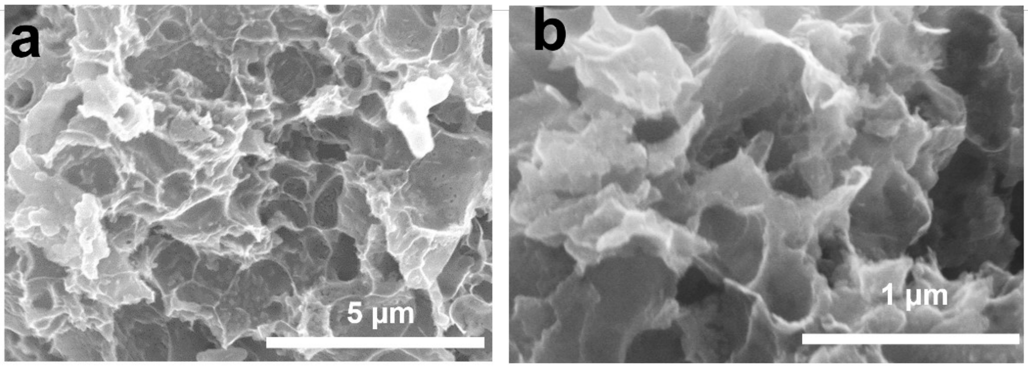

Figure S1. SEM images of SNC.

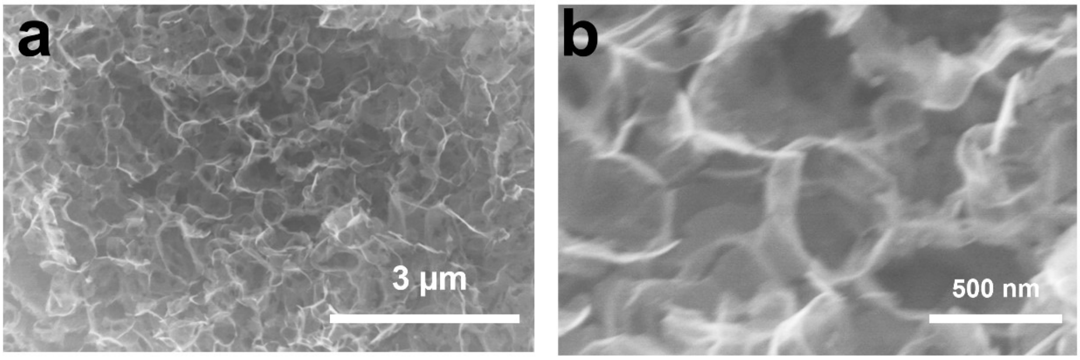

Figure S2. SEM images of NC.

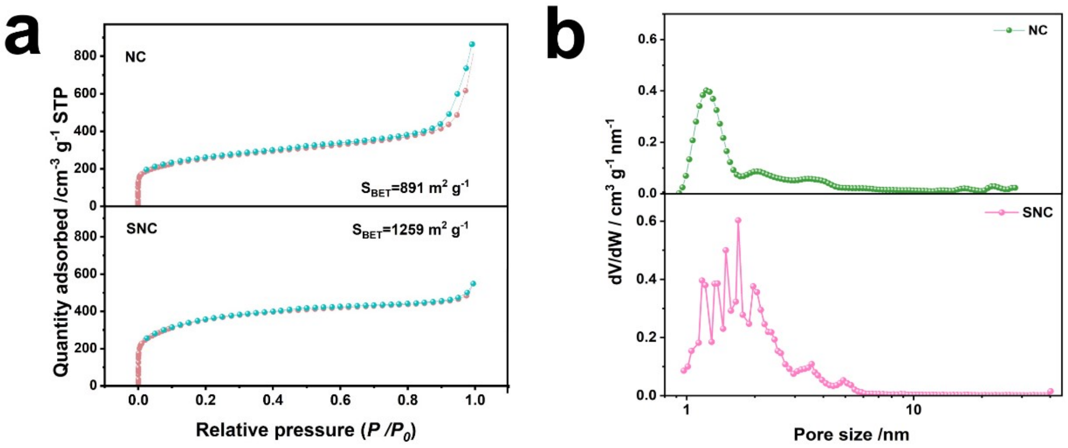

Figure S3. (a) N_2 absorption/desorption isothermals and (b) corresponding pore-size distribution curves of SNC and NC.

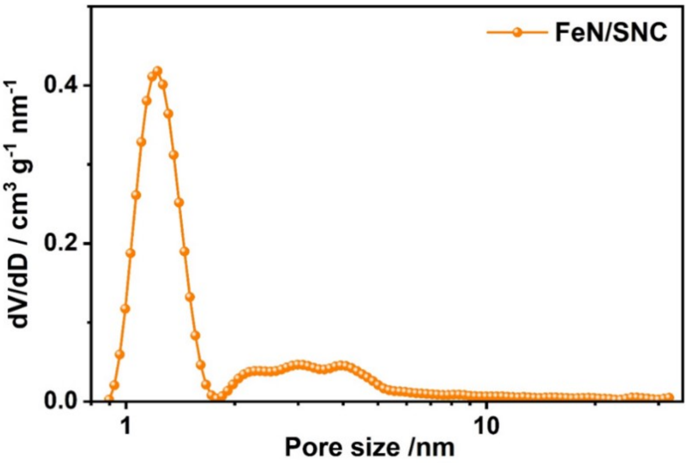

Figure S4. Pore-size distribution of FeN/SNC.

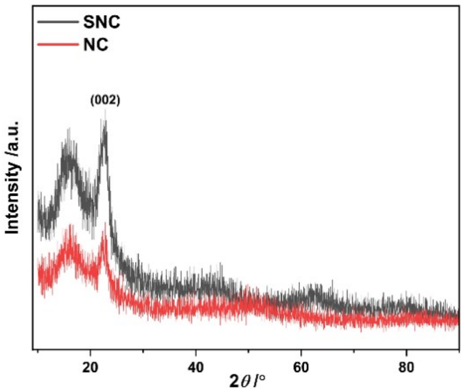

Figure S5. XRD patterns of SNC and NC.

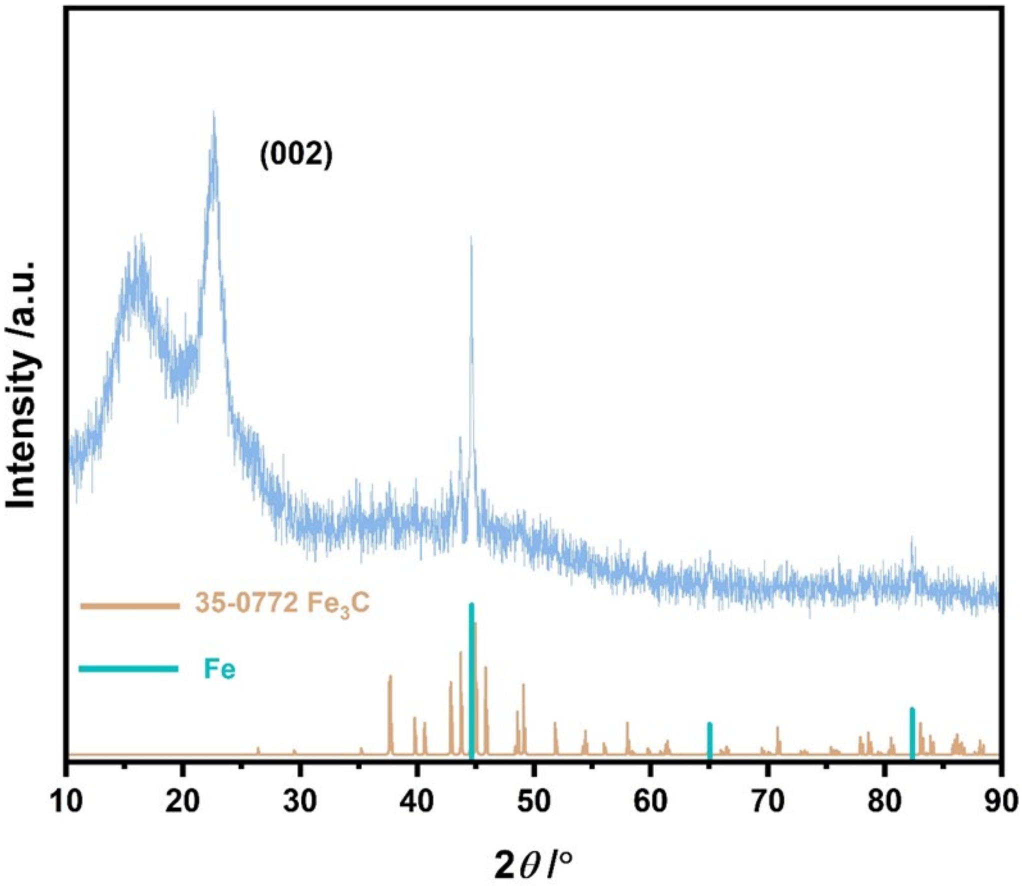

Figure S6. XRD pattern of FeN/SNC after the first pyrolysis.

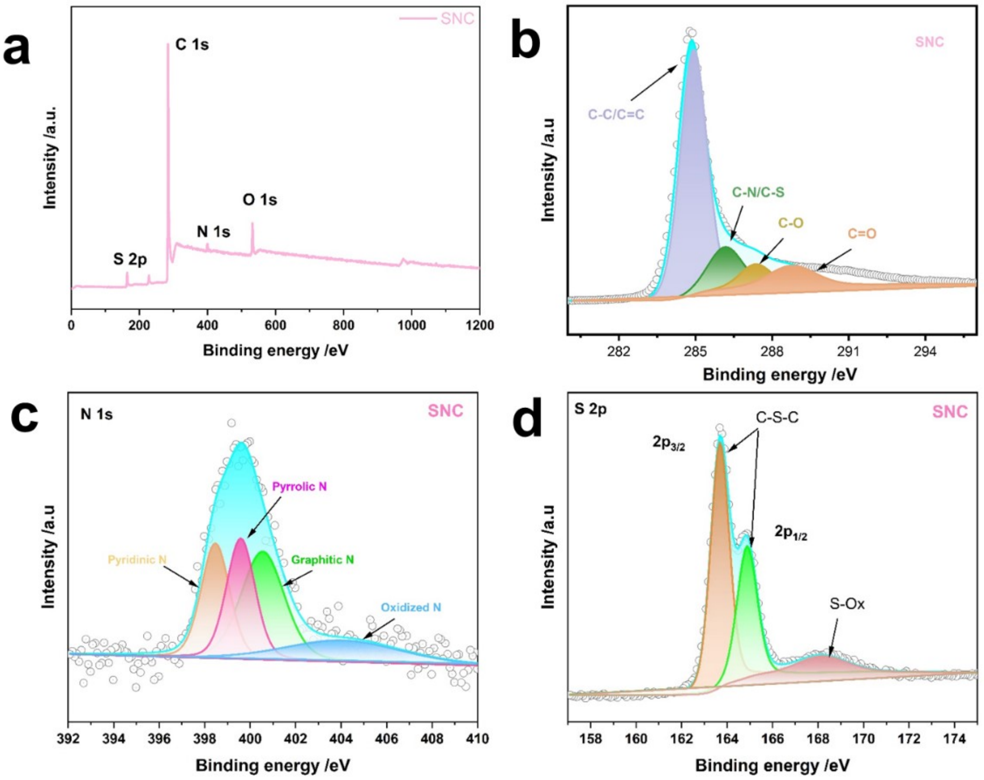

Figure S7. a) XPS survey spectrum of SNC. High-resolution b) C 1s, c) N 1s, and d) S 2p spectrum of SNC.

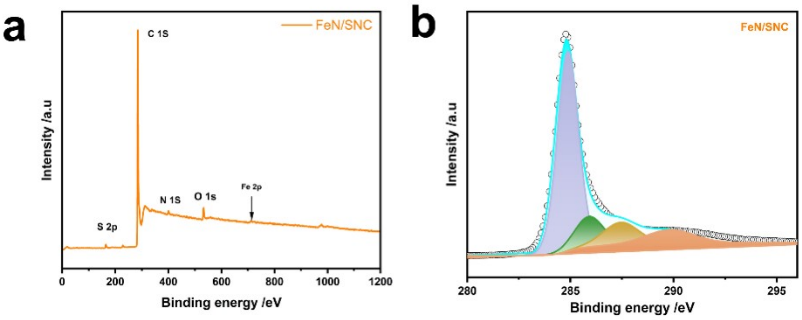

Figure S8. (a) XPS survey and (b) High-resolution C 1s XPS spectra of FeNC/SNC.

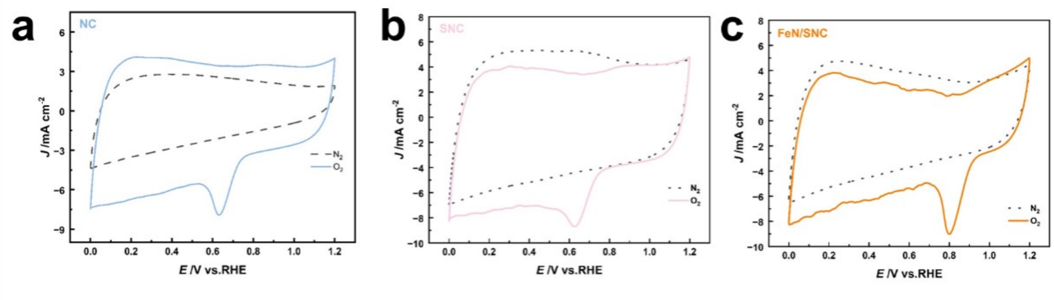

Figure S9. CV curves of different catalysts in N_2 (dashed line) and O_2-saturated (solid line) 0.1 M KOH solutions.

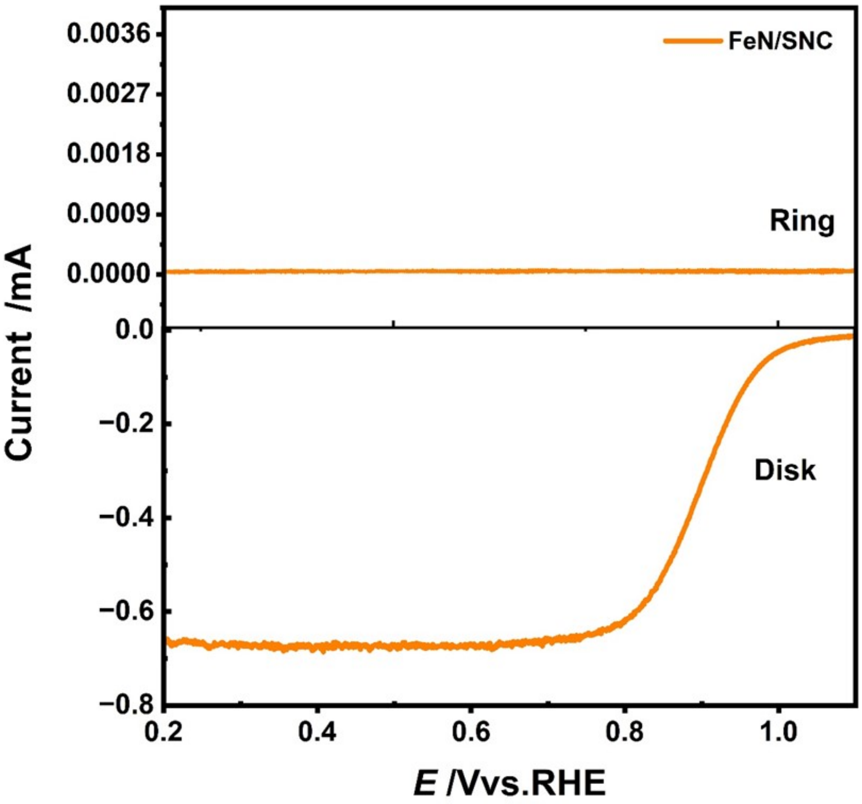

Figure S10. Ring (I_r) and disk (I_d) currents for FeN/SNC at 1600 rpm *via* an RRDE measurement.

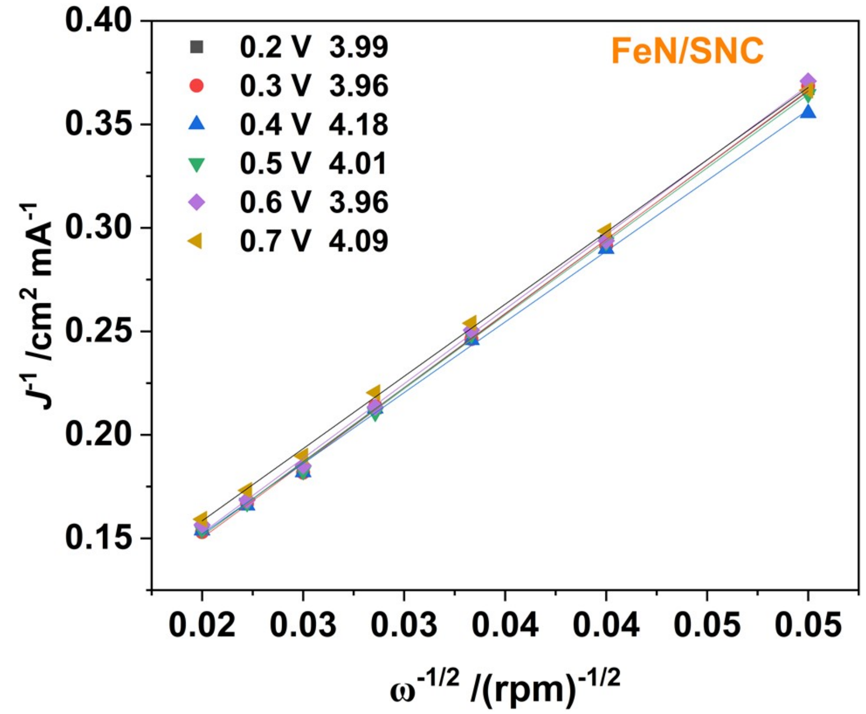

Figure S11. The corresponding K-L plots at various potentials

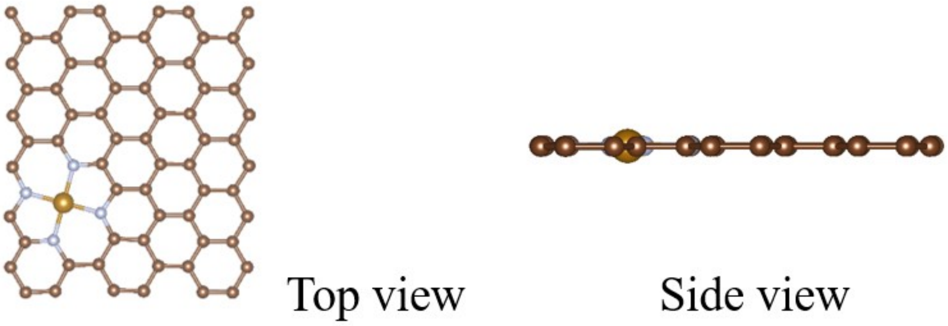

Figure S12. The optimized structure of Fe-N_4-C model.

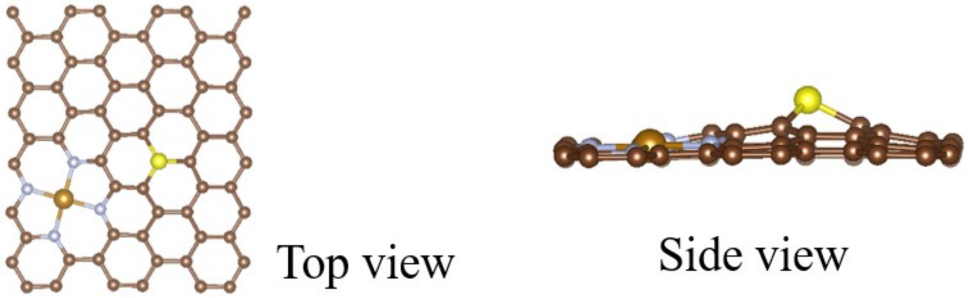

Figure S13. The optimized structure of Fe-N_4-C-S model.

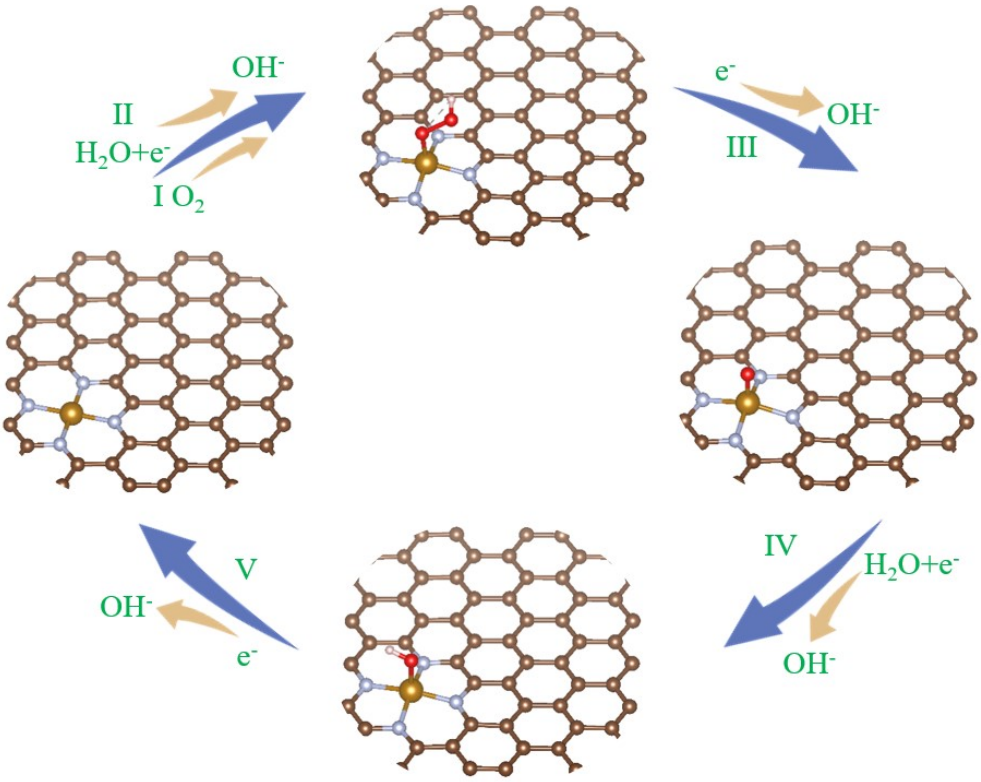

Figure S14. The optimized configurations of reaction intermediates for ORR on Fe-N_4-C model.

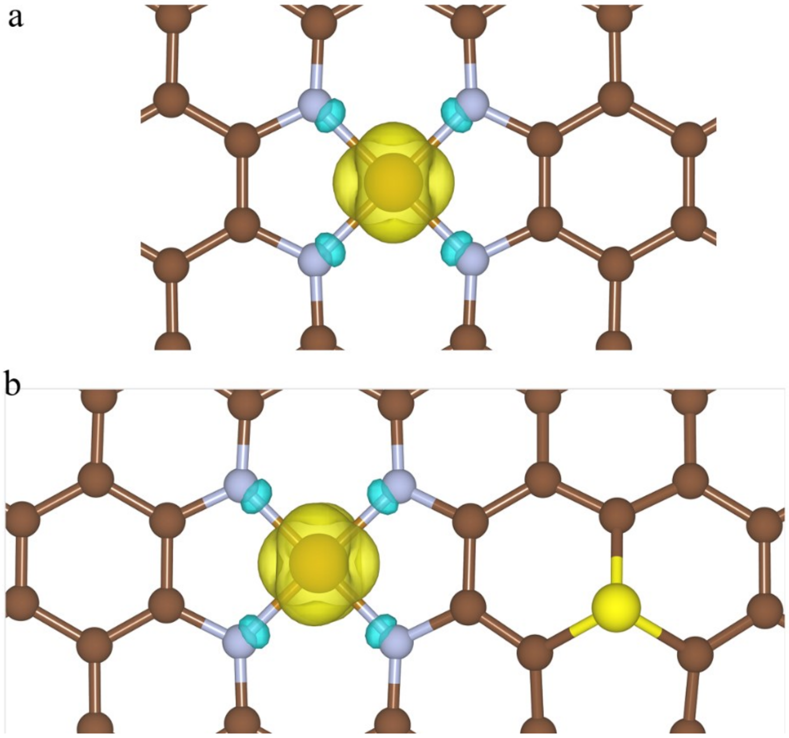

Figure S15. Spin density for the (a) Fe-N_4-C and (b) Fe-N_4-C-S models. The yellow and blue isosurfaces correspond to positive and negative spin densities, respectively, at an isosurface value of 0.005 e/$Å^3$.

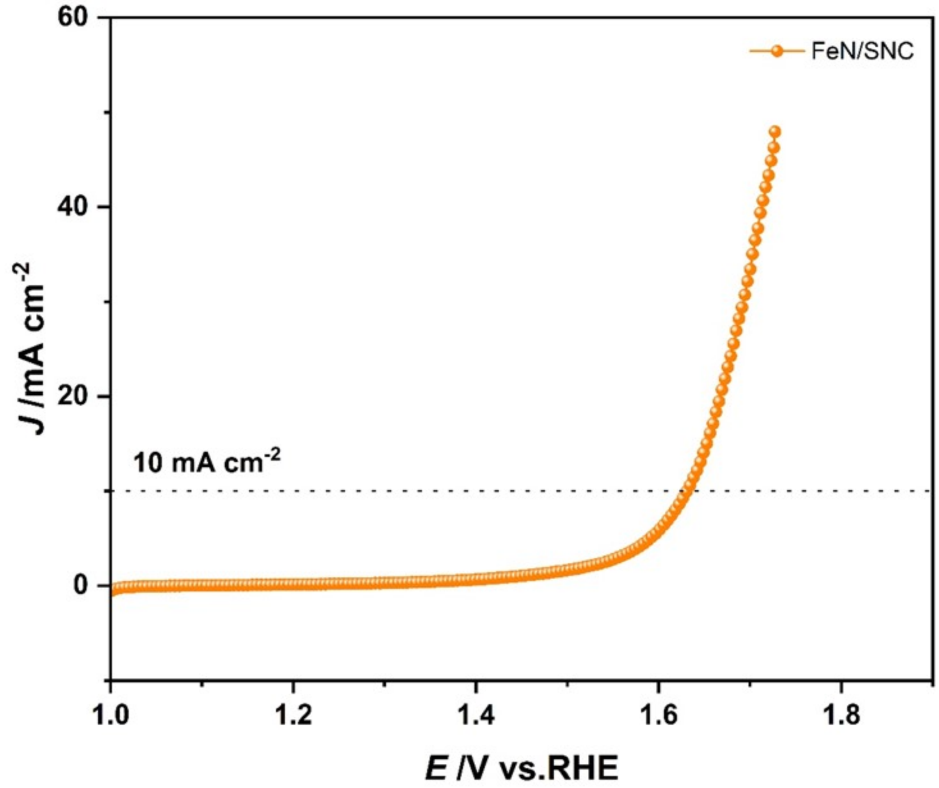

Figure S16. OER polarization curve of FeN/SNC in 1.0 M KOH.

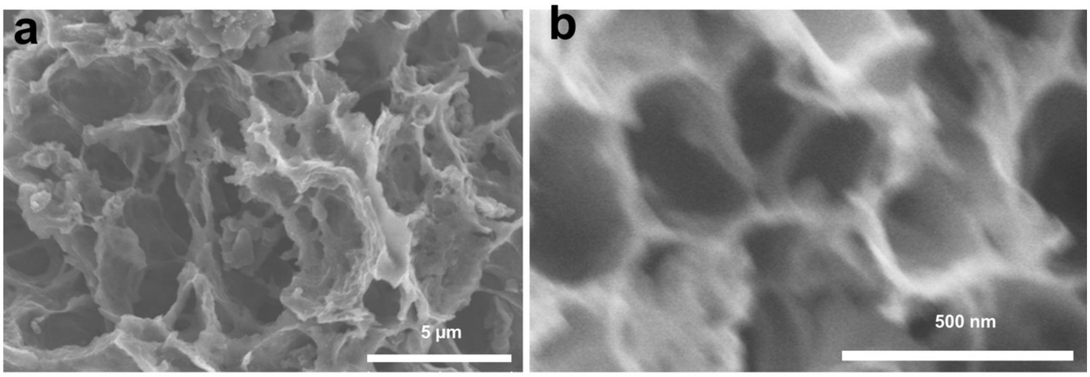

Figure S17. SEM images of $Ni(OH)_2$/FeN/SNC.

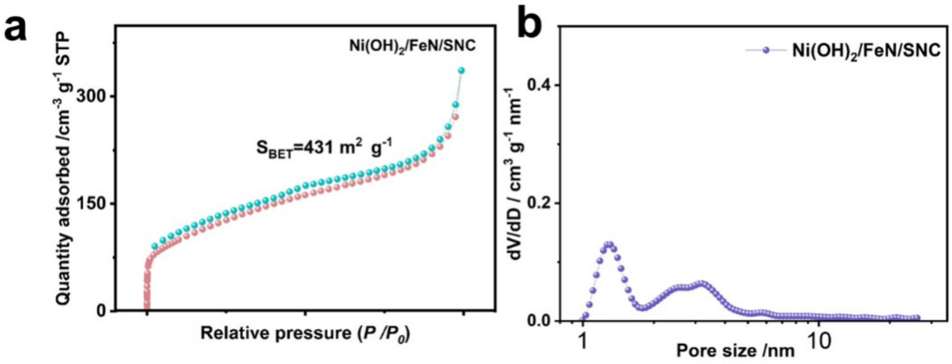

Figure S18. N_2 absorption/desorption isothermals and pore-size distribution of $Ni(OH)_2$/FeN/SNC

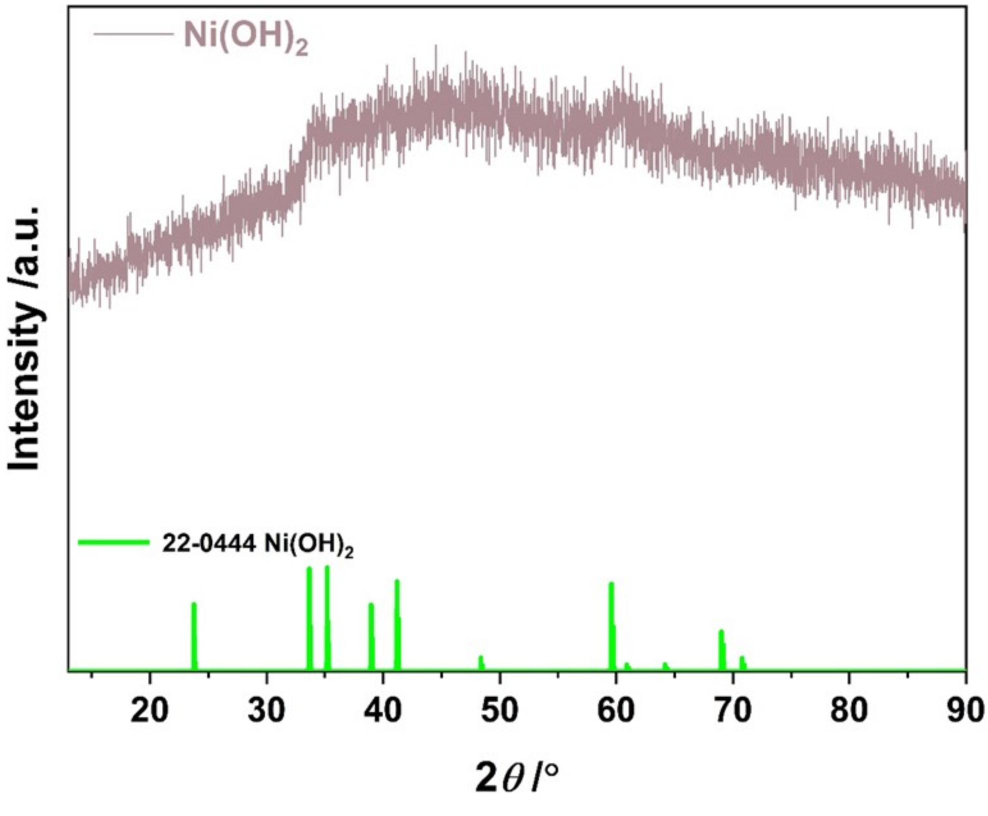

Figure S19. XRD pattern of as-prepared contrastive $Ni(OH)_2$.

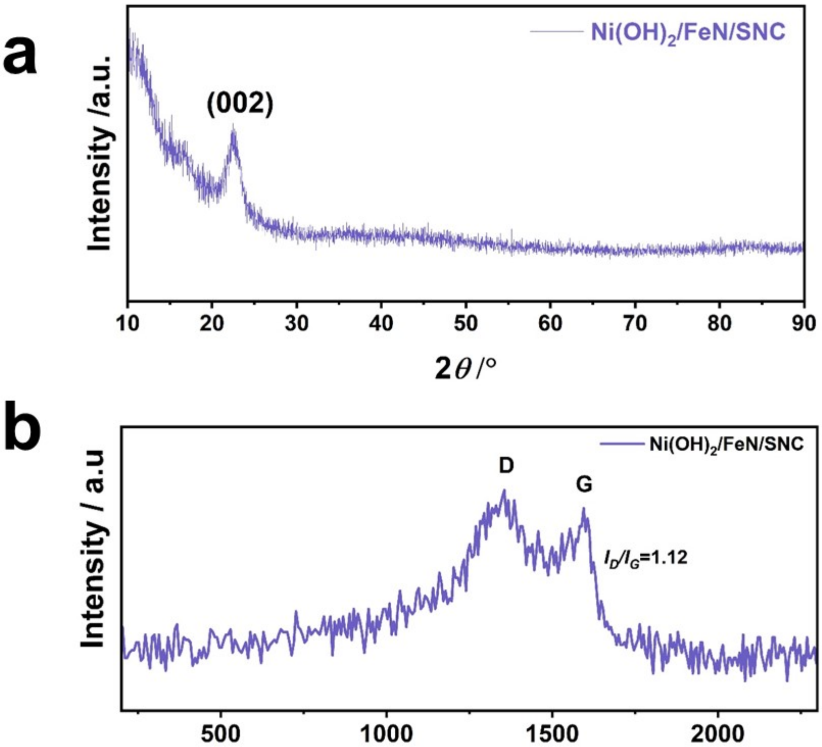

Figure S20. (a) XRD pattern and (b) Raman spectrum of $Ni(OH)_2$/FeN/SNC.

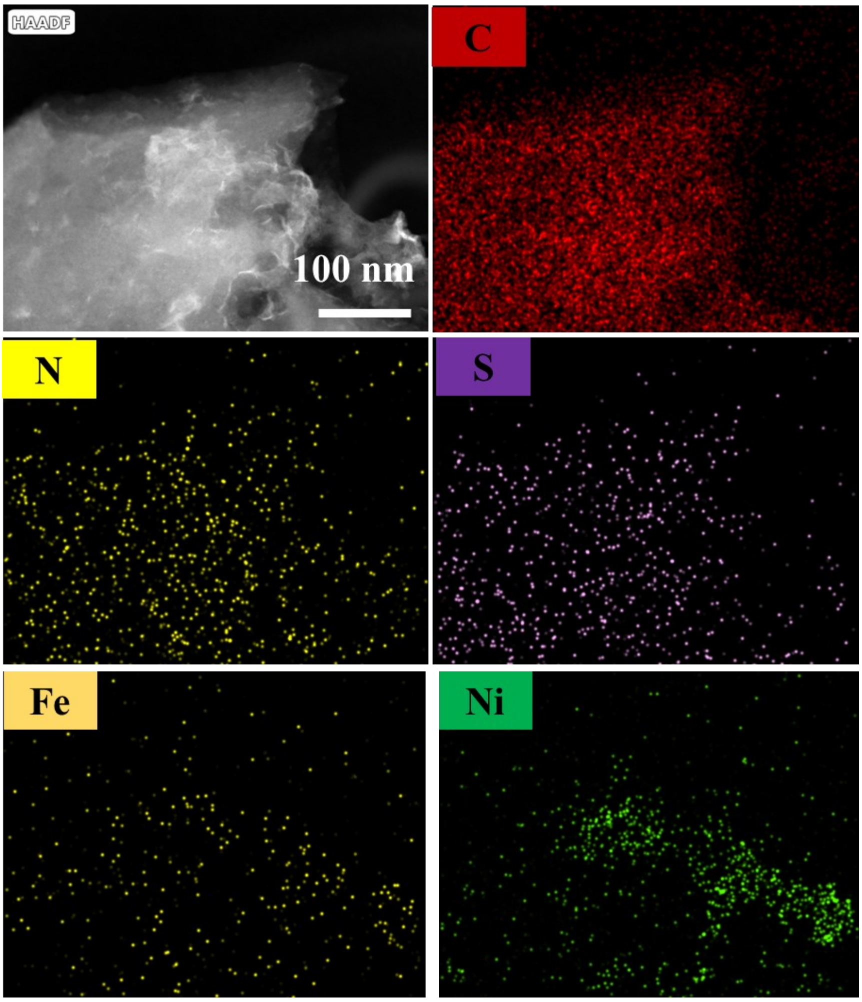

Figure S21. HAADF-STEM and corresponding element mapping images of $Ni(OH)_2$/FeN/SNC.

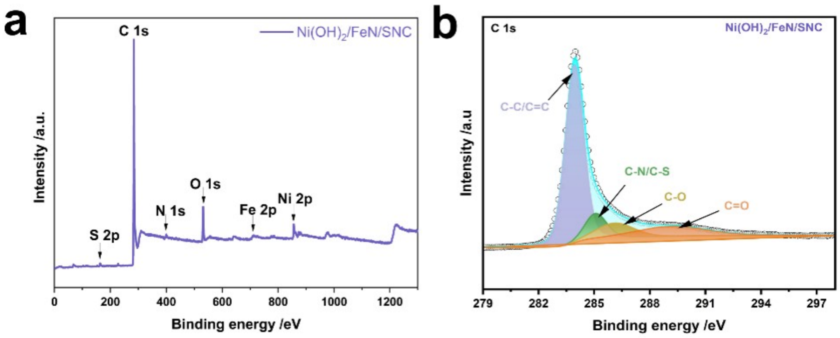

Figure S22. (a) XPS survey and (b) High-resolution C 1s XPS spectra of $Ni(OH)_2$/FeNC/SNC.

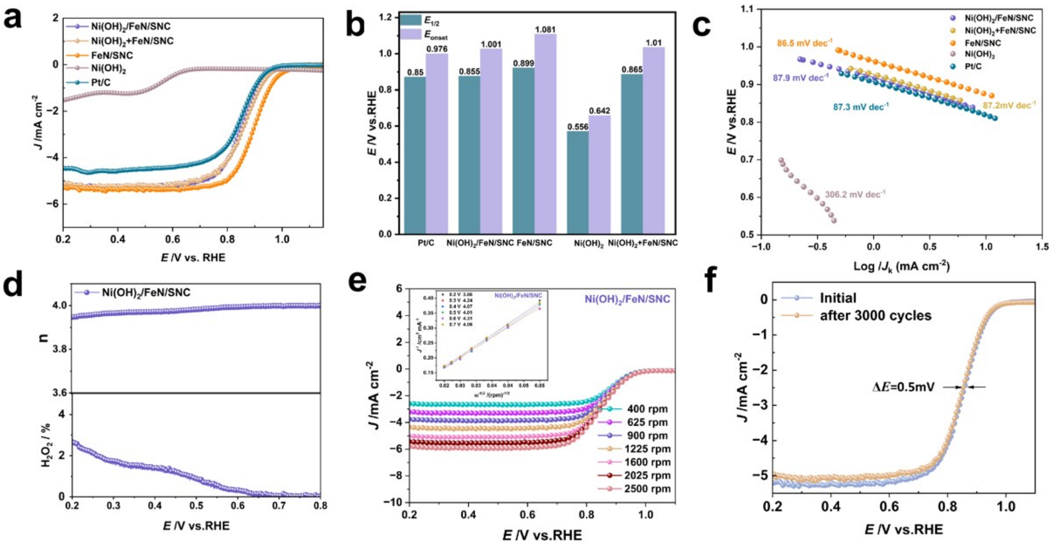

Figure S23. Evaluation of electrocatalytic performance for ORR. (a) LSV curves; b) Comparison of E_{onset} and $E_{1/2}$ of the catalysts; (c) Tafel plots; (d) Potential-dependent n (top) and H_2O_2 yield (bottom); (e) LSV curves in rotation speed ranges 400−2500 rpm. Inset: the corresponding K-L plots at various potentials; (f) LSV curves for Ni(OH)$_2$/FeN/SNC before and after 3000 cycles of CV.

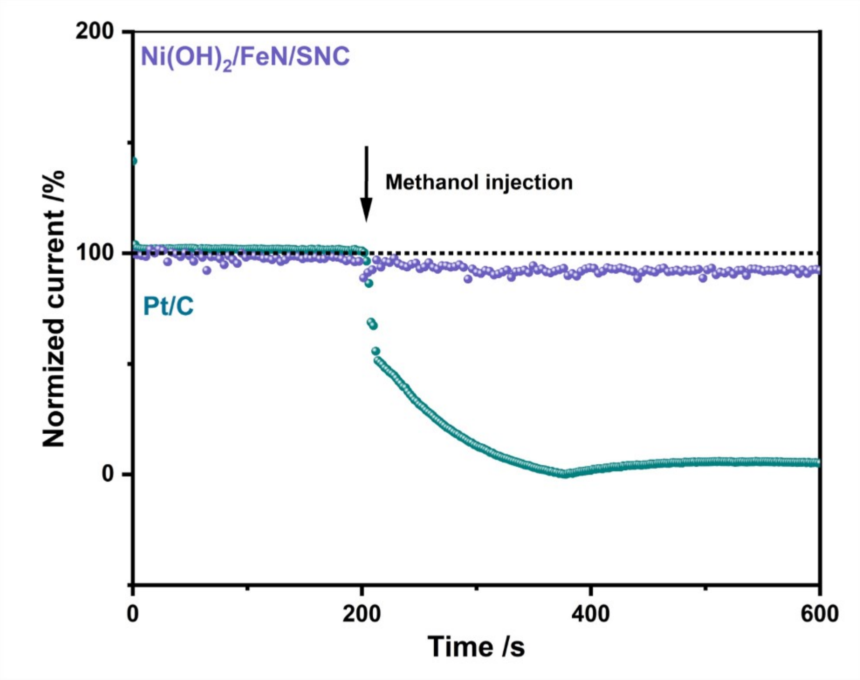

Figure S24. Methanol tolerance of Ni(OH)$_2$/FeNC/SNC at 0.7 V (*vs*. RHE) and a rotation speed of 1600 rpm.

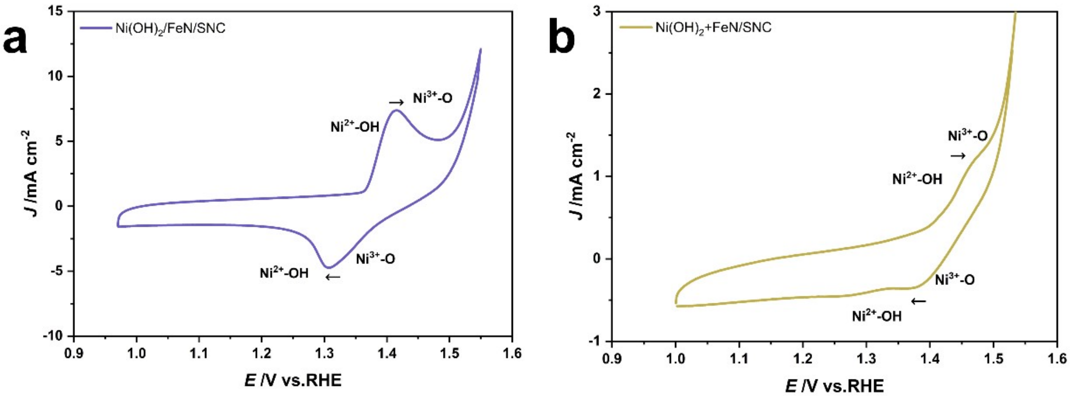

Figure S25. CV curves of Ni(OH)$_2$/FeN/SNC (a) and (b) Ni(OH)$_2$+FeN/SNC.

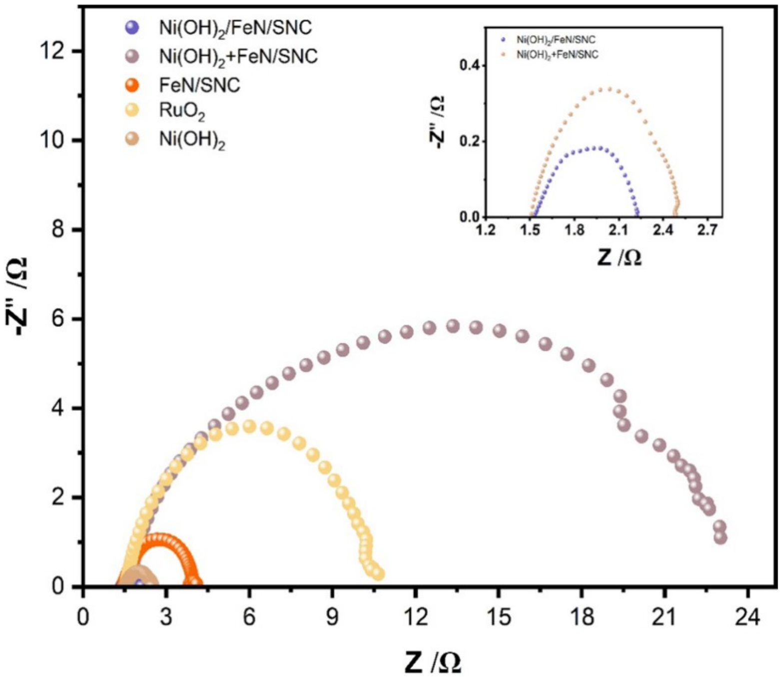

Figure S26. Nyquist plots of different catalsysts.

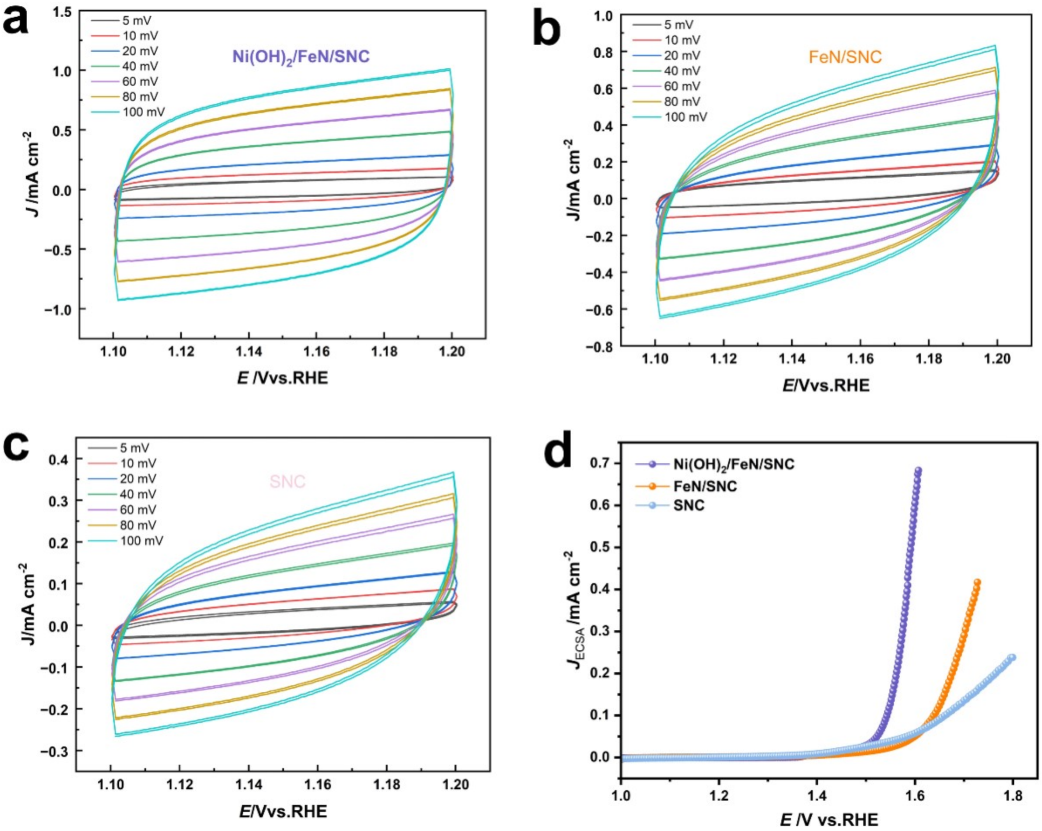

Figure S27. Cyclic voltammetry measured in the non-faradic region (1.10–1.20 V *vs*. RHE) at different scan rates (5-100 mV s^{-1}) for (a) Ni(OH)$_2$/FeN/SNC, (b) FeN/SNC and (c) SNC, respectively. (d) ECSA-normalized curves in 1.0 M KOH aqueous solution.

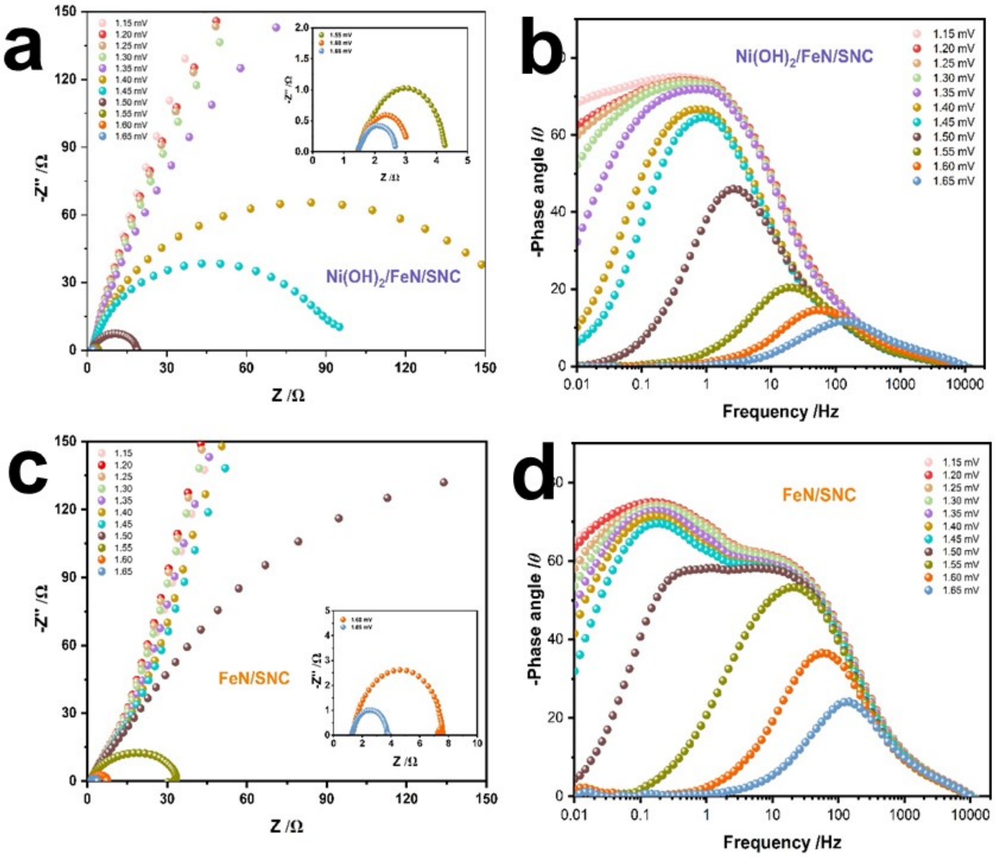

Figure S28. Electrochemical impedance spectra recorded in 1.0 M KOH at a series of potentials associated with OER: (a, c) Operando Nyquist plots, (b, d) Bode-phase plots.

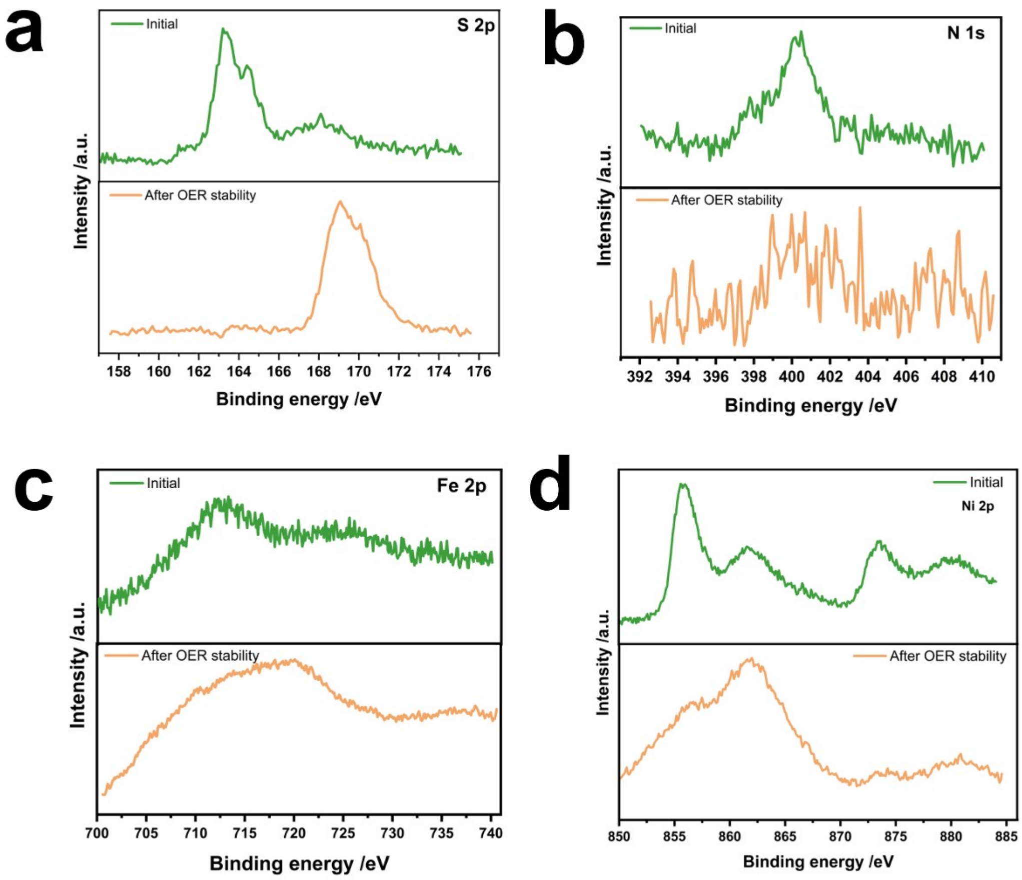

Figure S29. XPS spectra of Ni(OH)$_2$/FeNC/SNC before and after OER stability.

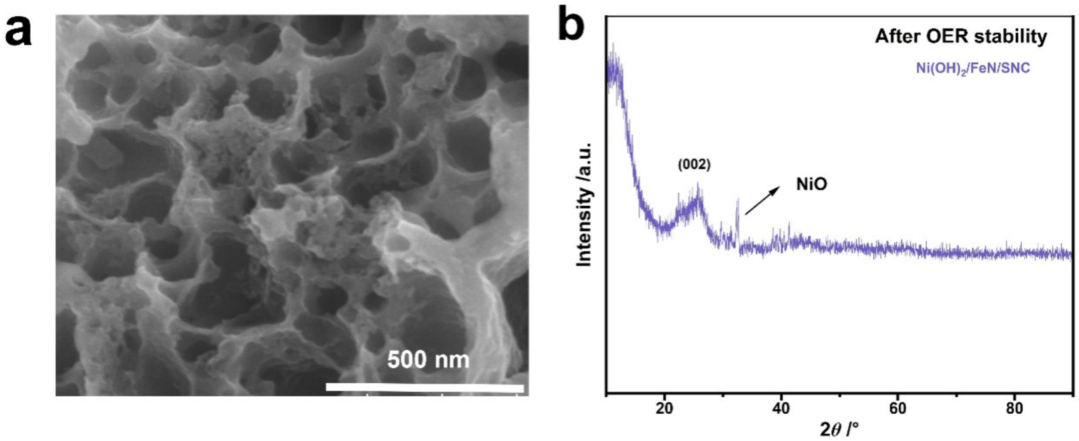

Figure S30. (a) SEM image and (b) XRD of Ni(OH)$_2$/FeNC/SNC after OER stability.

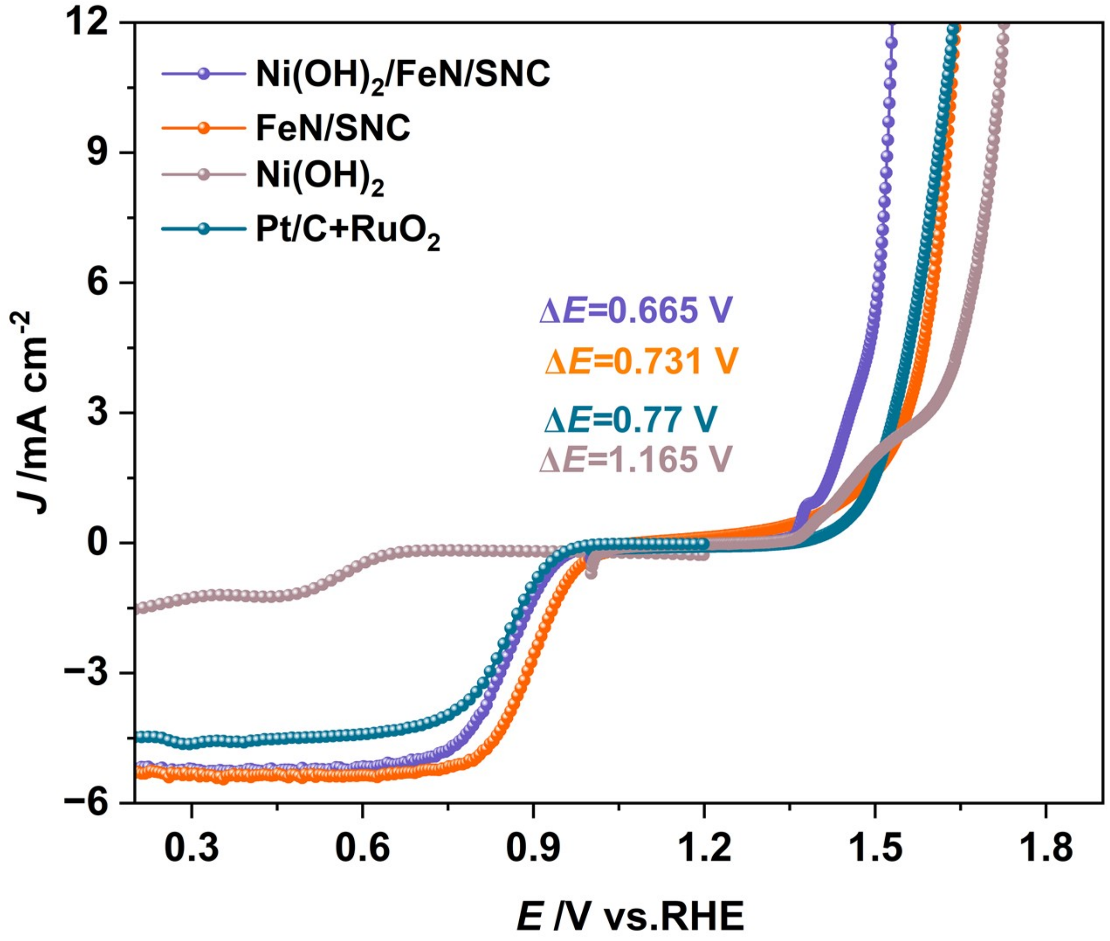

Figure S31. Polarization curves for ORR and OER bifunctional catalytic activities of different catalysts.

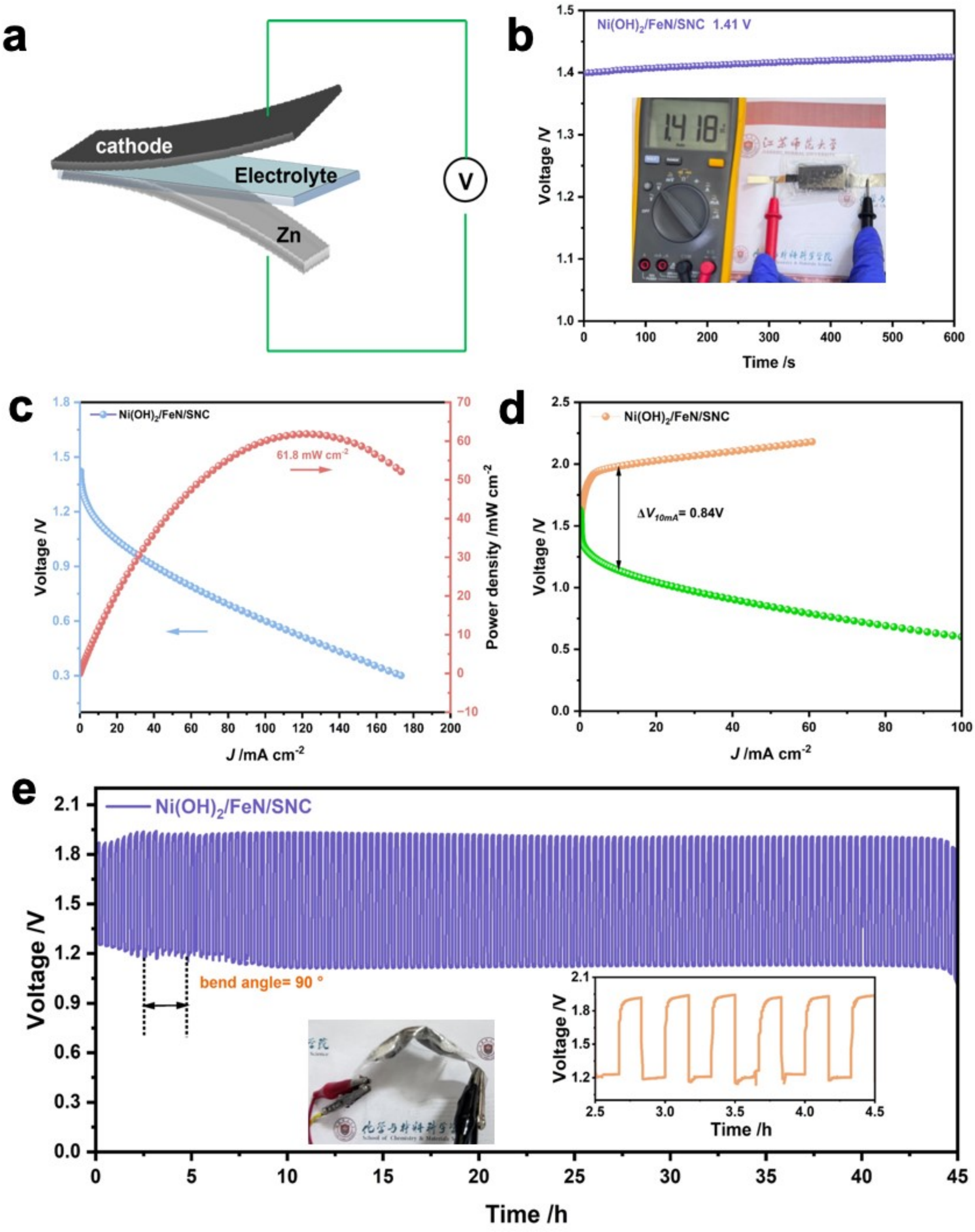

Figure S32. Quasi-solid-sate ZAB performance. (a) Schematic illustration of battery's configuration; (b) OCV curve. Inset shows that a multimeter tested the OCV; (c) Discharge polarization curve and corresponding power density curve; (d) Charge and discharge polarization curves; (e) Cycling stability at 1.0 mA cm^{-2}. Insets show the ZAB under deformation condition and corresponding charge–discharge curves.

Table S1. Summary of the Brunauer–Emmett-Teller (BET) surface area and pore size distributions of the as-prepared samples.

Samples	Specific surface area (m^2 g^{-1})	Micropore volume (cm^3 g^{-1})	Micropore size (nm)	Mesopore volume (cm^3 g^{-1})	Mesopore size (nm)
NC	891	0.190	1.453	0.996	2.974
SNC	1259	0.356	1.686	0.306	2.969
FeNC/SNC	652	0.164	1.266	0.299	2.98
$Ni(OH)_2$/FeNC/SNC	431	0.072	0.926	0.362	2.972

*Micropore and mesopore were determined using quenched solid density functional theory (QSDFT) method

Table S2. Mössbauer fitted parameters for the FeN/SNC

Fe species	**IS (mm s^{-1})**	**QS (mm s^{-1})**	**LW (mm s^{-1})**	**Relative absorption area (%)**	**Component (assignment)**
Singlet	-0.08946	-	0.41037	6.11	Param. or γ-Fe
Sextet1	0.75502	-0.13652	0.35712	34.60	Fe^{2+}-S
Sextet2	-0.06086	0	0.84222	12.05	α-Fe
Sextet3	0.19433	0.05606	0.33071	18.67	Fe_xC
Sextet4	0.34381	-0.18325	0.13485	2.86	Fe^{3+}-S
D1	0.32544	1.15056	0.79023	18.06	LS Fe^{II} N_4
D2	0.18122	3.34141	0.50000	4.45	MS $Fe^{II}N_4$
D3	1.81764	2.79712	0.44295	3.19	HS Fe^{II} N_4

IS: isomeric shift; QS: quadrupole splitting; LW: Line Width.

Table S3 Adsorption energies (eV) of ORR intermediates on the optimized structures at U=1.23 V

Model	O_2	$^*OOH$	$^*O$	$^*OH$	H_2O
Fe-N_4-C	0	-0.413	-1.436	-1.013	0
Fe-N_4-C-S	0	-0.49	-1.427	-0.91	0

Table S4 The *d*-band-center of Fe for different models

Model	Spin state	d-band-center (eV)
Fe-N_4-C	Spin-up	-3.512423
	Spin-down	-1.414624
Fe-N_4-C-S	Spin-up	-4.053392
	Spin-down	-2.704233

Table S5. The relative content of Fe-based species for FeNC/SNC and $Ni(OH)_2$/FeNC/SNC, determined by the deconvolution of Fe 2p XPS spectra.

	$Ni(OH)_2$/FeN/SNC		FeN/SNC	
	Fitted area	Relative content (%)	Fitted area	Relative content (%)
Fe^0	5745	18.4	1877	22.5
Fe^{2+}	6702	21.5	2572	30.8
Fe^{3+}	9200	29.5	1860	22.3
Sat.	9574	30.6	2033	24.4
total	31221	100	8342	100

Table S6. Comparison of performance parameters of bifunctional oxygen catalysts in this work with the results in references.

Electrocatalysts	$E_{1/2}$ (V)	E_{10} (V)	$\Delta E=E_{10}-E_{1/2}$ (V)	Power density /mW cm^{-2}	Reference
$Ni(OH)_2$/FeN/SNC	**0.855**	**1.52**	**0.665**	**145**	**this work**
$Ni(OH)_2$+FeN/SNC	**0.865**	**1.55**	**0.685**	\	**this work**
FeN/SNC	**0.899**	**1.63**	**0.731**	**148**	**this work**
$Ni(OH)_2$	**0.559**	**1.724**	**1.165**	\	**this work**
PtC/RuO_2	**0.85**	**1.62**	**0.77**	**113**	**this work**
CoNi@NCNT/CC-800	0.86	1.55	0.69	146	11
Fe_{800}-HZIF8	0.84	1.52	0.68	132.1	12
Co_9S_8/Fe-N-C	0.90	1.58	0.68	103	13
FeP/C-N-P0.28	0.90	1.567	0.667	118.5	14
Fe/Ni-NC@PDA	0.89	1.56	0.67	140.0	15
$Fe_{AD}Co_{NPs}$@NC-2	0.85	1.53	0.68	247.49	16
NiFe-LDH/SNC	0.825	1.528	0.703	100	17
NP Co_3O_4/Fe@C_2N	0.89	1.662	0.772	186.3	18

Co/CoO@HNC	0.83	1.66	0.83	85.6	19
Ni,Fe-DSAs/NCs	0.895	1.612	0.717	217.5	20
Co_2FeO_4/NCNTs	0.80	1.65	0.85	90.68	21
$MnCo_2O_4$/NCNTs	0.76	1.593	0.833	74.63	22
$CoFe_{1.6}Cr_{0.4}O_3S$	0.83	1.60	0.77	170	23
Mn@Co-NS	0.89	1.61	0.72	185.77	24
Fe−N−C/rGO	0.90	1.61	0.71	107.12	25
Fe/Ni−N−C	0.86	1.55	0.69	\	26
FeN_4B-NiN_4B	0.90	1.618	0.718	236.9	27

References:

1. T. D. Kühne, M. Iannuzzi, M. Del Ben, V. V. Rybkin, P. Seewald, F. Stein, T. Laino, R. Z. Khaliullin, O. Schütt, F. Schiffmann, D. Golze, J. Wilhelm, S. Chulkov, M. H. Bani-Hashemian, V. Weber, U. Borštnik, M.Taillefumier, A. S. Jakobovits, A. Lazzaro, H. Pabst, T. Müller, R. Schade, M. Guidon, S. Andermatt, N. Holmberg, G. K. Schenter, A. Hehn, A. Bussy, F. Belleflamme, G. Tabacchi, A. Glöß, M. Lass, I. Bethune, C. J. Mundy, C. Plessl, M. Watkins, J. VandeVondele, M. Krack and J. Hutter, *The Journal of Chemical Physics*, 2020, **152** (19), 194103.

2. J.VandeVondele, M. Krack, F. Mohamed, M. Parrinello, T. Chassaing and J. Hutter, *Computer Physics Communications*, 2005, **167** (2), 103-128.

3. J. P. Perdew, K. Burke and M. Ernzerhof, *Physical Review Letters*, 1996, **77** (18), 3865-3868.

4. S. Grimme, S. Ehrlich and L. Goerigk, *Journal of Computational Chemistry*, 2011, 32 (7), 1456-1465.

5. S. Grimme, J. Antony, S. Ehrlich and H. Krieg, *The Journal of Chemical Physics*, 2010, **132** (15), 154104.

6. S. Goedecker, M. Teter and J. Hutter, *Physical Review B*, 1996, **54** (3), 1703-1710.

7. J. VandeVondele and J. Hutter, *The Journal of Chemical Physics*, 2007, **127** (11), 114105.

8. C. Hartwigsen, S. Goedecker and J. Hutter, *Physical Review B*, 1998, **58** (7), 3641-3662.

9. T. Lu and F. W. Chen, *Journal of Computational Chemistry*, 2012, **33**, 580-592.

10. T. Lu, *The Journal of Chemical Physics*, 2024, **161**, 082503.

11. T. T. Qu, R. R. Liang, Z. A. Lu, Y. C. Du, X J. Han, J. B. Hou, M. Yang, K D. Cai,

and P. Xu, *ACS Applied Materials & Interfaces*, 2025, **17** (27), 39097-39107.

12 H. Z. Zhang, L. H. Chen, S. Wu, P. Zhang, H. Zhang, S. Tian, J. K. Li, X. Wang, G. H. Li, P. F. Wan and Q. L. Yang, Journal of Energy Storage, 2025, **137**, 118723.

13. M. Hong, Y. Y. Yang, J. H. Nie, X H. Zhang, W. J. Zhang, C. C. Du and Ji. H. Chen. Materials Today Physics, 2025, **54**, 101728.

14. Y. F. Su, H. M. Du, J. J.J Xu, J. S. Zhao, N. Q. Zhang, B. Lu, H. Yan, K. G. Qu and X. X. Zhang, Fuel, 2025, **387**, 134349.

15. S. Tian, L. H. Chen, S. Wu, J. K. Li, J. C. Yang, H. Z. Zhang, L. S. Wang, Y. Z. Sun, L. H. Wang, X. Y. Meng and Q. L. Yang, Chemical Engineering Journal, 2025, **520**, 166120.

16. M. Huo, Y. Liang, W. Liu, X. Zhang, K. Qin, Y. Ma, Z. Xing, J. Chang, G. Zhu, Adv. Energy Mater., 2024, 2405155.

17. L. Wang, J. Zhu, S. Zhu, L. Lu, P. Zhu, X. Zhao, S. Liu, ChemNanoMat, 2022, **8**, e202200242.

18. J. Kim, O. Gwon, O. Kwon, J. Mahmood, C. Kim, Y. Yang, H. Lee, J.H. Lee, H.Y. Jeong, J.B. Baek, G. Kim, ACS Nano, 2019, **13**, 5502-5512.

19. F. Zhang, L. Chen, Y. Zhang, Y. Peng, X. Luo, Y. Xu, Y. Shi, Chem. Eng. J., 2022, **447**, 137490.

20. Z. Wang, X. Jin, R. Xu, Z. Yang, S. Ma, T. Yan, C. Zhu, J. Fang, Y. Liu, S.J. Hwang, Z. Pan, H.J. Fan, ACS Nano, 2023, **17**, 8622-8633.

21. X. T. Wang, T. Ouyang, L. Wang, J. H. Zhong, T. Ma, Z. Q. Liu, Angew. Chem. Int. Ed., 2019, **58**, 13291.

22. Z. Wang, J. Huang, L. Wang, Y. Liu, W. Liu, S. Zhao, Z.Q. Liu, Angew. Chem. Int. Ed. 61, 2022, e202114696.

23. J. Sun, H. Xue, Y. Zhang, X. L. Zhang, N. Guo, T. Song, H. Dong, Y. Kong, J. Zhang, Q. Wang, Nano Lett., 2022, **22**, 3503.

24. X. Li, T. Zhou, Z. Luo, L. Zhang, Z. Ren, Q. Zhang, C. He, X. Jiang, Y. Li, X.

Ren, J. Alloys Compd., 2023, **939**, 168756.

25. L. Li, Y. Chen, H. Xing, N. Li, J. Xia, X. Qian, H. Xu, W. Li, F. Yin, G. He, H.Q. Chen, Nano Res., 2022, **15**, 8056−8064.

26. H. Li, J. Wang, R. Qi, Y. Hu, J. Zhang, H. Zhao, J. Zhang, Y. Zhao, Appl. Catal. B-Environ., 2021, **285**, 119778.

27. Z. Wang, R. Xu, Q. Ye, X. Jin, Z. Lu, Z. Yang, Y. Wang, T. Yan, Y. Liu, Z. Pan, S.J. Hwang, H.J. Fan, Adv. Funct. Mater., 2024, **34**, 2315376.